

Article

# Mechanochemical Defect Engineering of Nb<sub>2</sub>O<sub>5</sub>: Influence of LiBH<sub>4</sub> and NaBH<sub>4</sub> Reduction on Structure and Photocatalysis

Anna Michaely , Elias C. J. Gießelmann  and Guido Kickelbick \* 

Inorganic Solid-State Chemistry, Saarland University, Campus, Building C4.1, 66123 Saarbrücken, Germany

\* Correspondence: [guido.kickelbick@uni-saarland.de](mailto:guido.kickelbick@uni-saarland.de)

**Abstract:** Partial reduction of transition metal oxides via defect engineering is a promising strategy to enhance their electronic and photocatalytic properties. In this study, we systematically explored the mechanochemical reduction of Nb<sub>2</sub>O<sub>5</sub> using LiBH<sub>4</sub> and NaBH<sub>4</sub> as reducing agents. Electron paramagnetic resonance (EPR) spectroscopy confirmed a successful partial reduction of the oxide, as seen by the presence of unpaired electrons. Interestingly, larger hydride concentrations did not necessarily enable a higher degree of reduction as large amounts of boron hydrides acted as a buffer material and thus hindered the effective transfer of mechanical energy. Powder X-ray diffraction (PXRD) and <sup>7</sup>Li solid-state NMR spectroscopy indicated the intercalation of Li<sup>+</sup> into the Nb<sub>2</sub>O<sub>5</sub> lattice. Raman spectroscopy further revealed the increased structural disorder, while optical measurements showed a decreased band gap compared with pristine Nb<sub>2</sub>O<sub>5</sub>. The partially reduced samples showed significantly enhanced photocatalytic performance for methylene blue degradation relative to the unmodified oxides.

**Keywords:** black niobia; boron hydrides; mechanochemistry; reduction; solid-state reactions



Academic Editor: Claudio Ferrari

Received: 14 April 2025

Revised: 14 May 2025

Accepted: 19 May 2025

Published: 26 May 2025

**Citation:** Michaely, A.; Gießelmann, E.C.J.; Kickelbick, G. Mechanochemical Defect Engineering of Nb<sub>2</sub>O<sub>5</sub>: Influence of LiBH<sub>4</sub> and NaBH<sub>4</sub> Reduction on Structure and Photocatalysis. *Solids* **2025**, *6*, 26. <https://doi.org/10.3390/solids6020026>

**Copyright:** © 2025 by the authors. Licensee MDPI, Basel, Switzerland. This article is an open access article distributed under the terms and conditions of the Creative Commons Attribution (CC BY) license (<https://creativecommons.org/licenses/by/4.0/>).

## 1. Introduction

Transition metal oxides (TMOs), such as Nb<sub>2</sub>O<sub>5</sub>, are notable for their diverse oxidation states and advantageous electronic and optical properties, making them suitable for applications in energy storage and photocatalysis. Hereby, Nb<sub>2</sub>O<sub>5</sub> is a stable wide-band gap *n*-type semiconductor, whose properties strongly depend on the type of polymorph. Among these polymorphs monoclinic H-Nb<sub>2</sub>O<sub>5</sub> is the thermodynamically stable variant and consists of a ReO<sub>3</sub> block-type structure of 3 × 5 and 3 × 4 blocks of corner-sharing NbO<sub>6</sub> octahedra within the blocks and edge sharing between blocks [1]. With a band gap ranging from 3.1 to 3.9 eV [2,3] and an electrical conductivity of 10<sup>-13</sup>–10<sup>-6</sup> S cm<sup>-1</sup> [4], Nb<sub>2</sub>O<sub>5</sub> has been primarily explored for sensor applications and various electronic devices [5,6], with some studies also investigating its potential in dye-sensitized solar cells [7] and photocatalytic processes [8].

Upon partial reduction of TMOs and the creation of oxygen vacancies, their electronic properties can be enhanced compared with the pristine oxides, yielding materials with improved chemical and physical characteristics [9]. For instance, Chen et al. synthesized so-called black titania through hydrogenation of TiO<sub>2</sub>, which introduced defects and partially reduced Ti<sup>4+</sup> cations to Ti<sup>3+</sup>, resulting in increased photocatalytic activity relative to the pristine oxide [10]. This approach has spurred interest in defect engineering within TMOs, leading to reports on partially reduced oxides such as Nb<sub>2</sub>O<sub>5-x</sub> [11,12], ZrO<sub>2-x</sub> [13], WO<sub>3-x</sub> [14], V<sub>2</sub>O<sub>5-x</sub> [15], and MoO<sub>3-x</sub> [16], which also exhibit enhanced light

absorption [13], as well as improved photocatalytic [15] and photoelectrochemical (PEC) activities [11,12].

Despite the potential of black Nb<sub>2</sub>O<sub>5</sub>, its synthesis has not been extensively studied. Common synthesis methods involve high-temperature reductions using aluminum [11,12] or NaBH<sub>4</sub> [17] as reducing agents, or the creation of oxygen vacancies by the diffusion-reduction method [18], resulting in the formation of high-performance materials for photoelectrochemical water-splitting, sodium-ion batteries, and photocatalytic CO<sub>2</sub> reduction, respectively. However, these methods often require energy-intensive annealing steps under inert gas [19], hydrogen [20–22], or vacuum [23] conditions to induce partial reduction and formation of Nb<sub>2</sub>O<sub>5-x</sub>.

In contrast, mechanochemical approaches offer a more energy-efficient alternative by inducing chemical reactions through the absorption of mechanical energy at room temperature [24]. While energy consumption is heavily reduced with this method, the continuous impact of milling balls also results in the creation of additional defects and an increase in reactivity. Literature on mechanochemical reduction of TMOs is limited and includes the use of either highly reactive alkaline metals, such as Na [25] or Li [26], or non-conventional hydrides such as TiH<sub>2</sub> [27]. In a recent study, we were able to show that alkali metal hydrides LiH and NaH represent readily available and powerful reducing agents for the partial reduction in a ball mill of rutile type TiO<sub>2</sub> and monoclinic H-Nb<sub>2</sub>O<sub>5</sub>, resulting in the formation of black TiO<sub>2</sub> and black Nb<sub>2</sub>O<sub>5</sub> with enhanced photocatalytic activities for the degradation of methylene blue [28].

Building on this knowledge, we systematically investigated the effectiveness of LiBH<sub>4</sub> and NaBH<sub>4</sub>, which had already been used in high temperature reductions, as reducing agents in mechanochemical reduction processes. More specifically, the effects of concentration and milling duration on the resulting materials' photocatalytic activity for methylene blue degradation were examined.

## 2. Materials and Methods

### 2.1. Materials

Nb<sub>2</sub>O<sub>5</sub> (ChemPur, Karlsruhe, Germany, 99.98%), NaBH<sub>4</sub> (Merck, Hohenbrunn, Germany, ≥98%), and LiBH<sub>4</sub> (Sigma Aldrich, Steinheim, Germany, ≥95%) were used without further purification and stored in a glovebox under argon atmosphere. 1,2-dimethoxyethane (ABCR GmbH, Karlsruhe, Germany, 99%) was dried in a solvent-purifying system SPS 5 (MBRAUN, Garching, Germany). All solids were characterized by X-ray diffraction before use.

### 2.2. Synthesis

The syntheses were performed in a Pulverisette 7 (Fritsch, Idar-Oberstein, Germany) planetary ball mill using ZrO<sub>2</sub> grinding jars with a volume of 45 mL, and 180 ZrO<sub>2</sub> milling balls with a diameter of 5 mm. All syntheses were carried out under an argon atmosphere using the glovebox technique. In a typical experiment, 3.00 g of Nb<sub>2</sub>O<sub>5</sub> (11.29 mmol, 1 eq.) was milled with *n* eq. of ABH<sub>4</sub> (*n* = 0.25, 0.5, 1, and 2; A = Li, Na). The milling speed was set to 300 rpm, while the milling time was equal to 10, 30, and 60 min. To prevent cementation during the milling process with 1 or 2 eq. of ABH<sub>4</sub>, 200 µL of dry 1,2-dimethoxyethane (DME) was added.

Afterwards, the samples were washed with water and MeOH several times to remove unreacted alkali metal hydrides as well as side-products. Both solvents were degassed with argon for 1 h beforehand. After centrifugation, samples were dried in a vacuum oven at 80 °C and stored in an argon-filled glovebox.

### 2.3. Testing of the Photocatalytic Activity

The photocatalytic experiments were performed in an EvoluChem™ PhotoRedOx Box (HepatoChem, Beverly, MA, USA) equipped with a 2 × 20 mL sample holders, an EvoluChem 365PF lamp (365 nm) for testing the photocatalytic activity in the UV region, and an EvoluChem 6200PF lamp (cold white) for the Vis region.

In a typical methylene blue (MB) degradation experiment, 15 mg of catalyst (1 mg/mL) was added to 15 mL of an aqueous MB solution (20 ppm). After stirring for 30 min in the dark, the suspensions were irradiated. After certain time intervals, 0.4 mL of suspension was periodically sampled and centrifuged to separate the photocatalyst from the solution. The MB solution was then diluted by a factor of 2 before the concentration of MB was measured by UV–Vis spectroscopy.

### 2.4. Characterization

Powder X-ray diffraction (PXRD) patterns were recorded on a D8-A25-Advance diffractometer (Bruker-AXS, Karlsruhe, Germany) under ambient conditions in Bragg–Brentano  $\theta$ - $\theta$ -geometry (goniometer radius 280 mm) with Cu  $K_{\alpha}$ -radiation ( $\lambda = 154.0596$  pm). A 12  $\mu\text{m}$  Ni foil served as a  $K_{\beta}$  filter at the primary beam side. At variable divergence slit was mounted at the primary beam side and a LYNXEYE detector with 192 channels at the secondary beam side. Experiments were carried out in a  $2\theta$  range of 7 to 120° with a step size of 0.013° and a total scan time of 2 h. Rietveld refinement of the recorded diffraction patterns was performed using TOPAS 5.0 software [29]. Crystallographic structure and microstructure were refined, while instrumental line broadening was included in a fundamental parameters approach [30]. The mean crystallite size  $\langle L \rangle$  was calculated as the mean volume weighted column height derived from the integral breadth. Crystal structure data were obtained from the Pearson's Crystal database [31].

EPR spectra were recorded using an Elecsys E580 X-band spectrometer (Bruker, Ettlingen, Germany) with an ER 4118X-MD5 resonator (Bruker, Ettlingen, Germany). All shown EPR spectra were recorded at 80 K using a closed cycle cryostat Cryogenic CF VTC (Cryogenic Limited, London, United Kingdom).

For the acquisition of the Raman spectra, a Raman microscope LabRAM HR Evolution HORIBA Jobin Yvon A (Horiba, Longmujeau, France) with a 633 nm He–Ne laser (Melles Griot, IDEX Optics and Photonics, Albuquerque, NM, USA) and a 1800 lines/mm grating was used.

UV–Vis diffuse reflectance spectra were performed on a Perkin Elmer Lambda 750 spectrometer (PerkinElmer Inc., Shelton, CT, USA) equipped with a 100 mm integration sphere from 290 to 1500 nm with a 2 nm increment and an integration time of 0.2 s. BaSO<sub>4</sub> was used as the reference.

<sup>7</sup>Li and <sup>11</sup>B single-pulse excitation magic angle spinning (SPE MAS) NMR spectra were recorded at 155.57 MHz and 128.43 MHz, respectively, on a Bruker AV400WB spectrometer (Bruker, Billerica, MA, USA) at 298 K in standard ZrO<sub>2</sub> rotors with a diameter of 4 mm. A spinning rate of 13 kHz and a relaxation delay of 3 s were applied. Solid LiCl and NaBH<sub>4</sub> were used as an external reference with a chemical shift of 0 and −42 ppm, respectively. Spectra were recorded using the TopSpin software [32]. Fitting of the spectra was performed using the DMFit software program package [33]. The extracted data were compiled in the Supplementary Materials, Table S1.

## 3. Results

### 3.1. Reduction Process During Ball Milling

For the mechanochemically induced partial reduction of Nb<sub>2</sub>O<sub>5</sub>, niobia was milled with  $n$  equivalents of LiBH<sub>4</sub> and NaBH<sub>4</sub> ( $n = 0.25, 0.5, 1, \text{ and } 2$  eq.) for 10, 30, and 60 min at

a constant milling speed of 300 rpm. To prevent cementation and ensure a homogeneous reaction mixture, 200  $\mu\text{L}$  DME was added during milling with 1 and 2 eq. of  $\text{MBH}_4$  for 60 min.

After just 10 min of mechanochemical treatment at room temperature, a color change from white  $\text{Nb}_2\text{O}_5$  to light gray and dark blue-black was observed depending on the milling conditions (Supplementary Materials, Figure S1). This change in color can be attributed to the reduction of  $\text{Nb}^{5+}$  to  $\text{Nb}^{4+}$  [34] accompanied by the intercalation of alkali metal ions and/or the presence of color centers [35] due to the formation of oxygen vacancies [36] to maintain electroneutrality. The formation of unpaired electrons, which confirmed a successful reduction [12,37], was proven by EPR spectroscopy even for the lighter-colored  $\text{NaBH}_4$ -reduced samples (Figure 1a). Hereby,  $\text{LiBH}_4$  produced darker (anthracite to blackish blue) and more reduced samples than  $\text{NaBH}_4$  (light gray to darker gray). To monitor the evolution of the pressure inside the milling jar, the EASY GTM system by Fritsch was used. As shown in Figure 1b, a continuous pressure increases up to 0.4 and 1.6 bar was observed with  $\text{NaBH}_4$  and  $\text{LiBH}_4$ , respectively, which was also observed due to hydrogen formation during the mechanochemical reduction of  $\text{Nb}_2\text{O}_5$  with  $\text{NaH}$  and  $\text{LiH}$  [28]. In theory, the formation of volatile borane species as side-products was also conceivable, but not further investigated, as the focus lay on the characterization of the as-prepared reduced oxides. The higher pressure observed with  $\text{LiBH}_4$  aligned with its greater efficiency in achieving reduction compared with  $\text{NaBH}_4$ . The milling process also elevated the temperature but remained below  $35^\circ\text{C}$  for both hydrides.

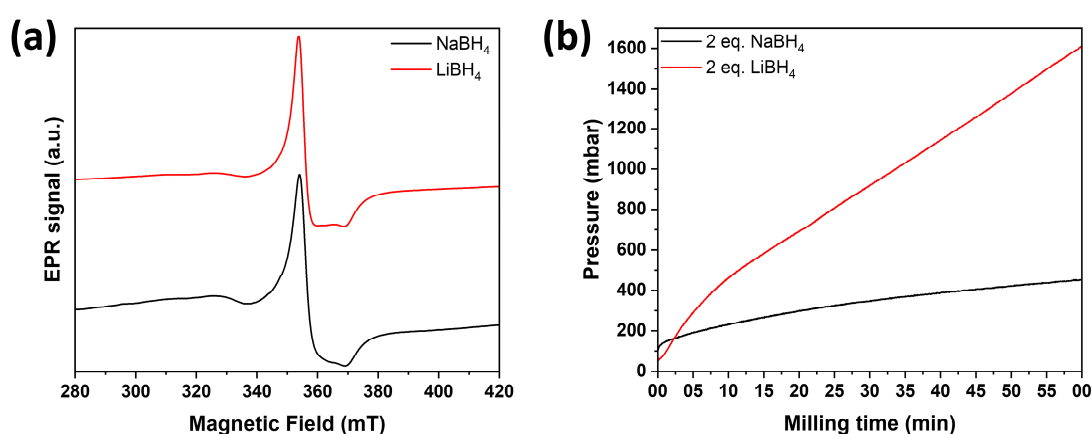


**Figure 1.** (a) Normalized continuous wave (CW) EPR spectra of  $\text{Nb}_2\text{O}_5$  reduced with 0.25 eq.  $\text{NaBH}_4$  (black) and 0.25 eq.  $\text{LiBH}_4$  (red) for 60 min. (b) Evolution of the pressure inside the milling jar for the reaction of  $\text{Nb}_2\text{O}_5$  with 2 eq.  $\text{NaBH}_4$  (black) and  $\text{LiBH}_4$  (red).

### 3.2. PXRD Analysis and Influence of the Hydride Concentration on the Reduction

Powder X-ray diffraction (PXRD) analysis was conducted to assess structural modifications induced by partial reduction during milling. The diffraction patterns of all reduced samples remained consistent with monoclinic  $\text{H-Nb}_2\text{O}_5$  (space group  $P2/m$ ), indicating no major structural transformation, regardless of the reducing agent, its concentration, or the milling duration (Figure 2a; Supplementary Materials, Figures S2–S8). However, a distinct shift toward lower diffraction angles was observed for all  $\text{LiBH}_4$ -reduced samples (Figure 2b). Rietveld refinement revealed an expansion of the unit cell volume of by up to  $\sim 6 \times 10^{-3} \text{ nm}^3$  in these samples compared with pristine  $\text{Nb}_2\text{O}_5$ , whereas no significant increase was detected for  $\text{NaBH}_4$ -reduced samples (Figure 2c). Generally, higher  $\text{LiBH}_4$  concentrations resulted in increased cell volumes, while the milling time had a rather low influence. As previously reported for the mechanochemical reduction of transition metal oxides using  $\text{LiH}$  and  $\text{NaH}$  [28], the observed volume increase was attributed to  $\text{Li}^+$

intercalation, given its smaller ionic radius of (76 pm) compared with  $\text{Na}^+$  (102 pm) [38]. Based on the unit cell expansion, the estimated composition of the  $\text{LiBH}_4$ -reduced samples ranged from  $\text{Li}_{0.06(1)}\text{Nb}_2\text{O}_5$  to  $\text{Li}_{0.13(1)}\text{Nb}_2\text{O}_5$  (Figure 2c). In contrast, previously reported  $\text{LiH}$ -reduced samples exhibited a broader composition range ( $\text{Li}_{0.02(1)}\text{Nb}_2\text{O}_5$  to  $\text{Li}_{0.25(1)}\text{Nb}_2\text{O}_5$ ) [28], consistent with the higher reactivity of  $\text{LiH}$  compared with  $\text{LiBH}_4$ .

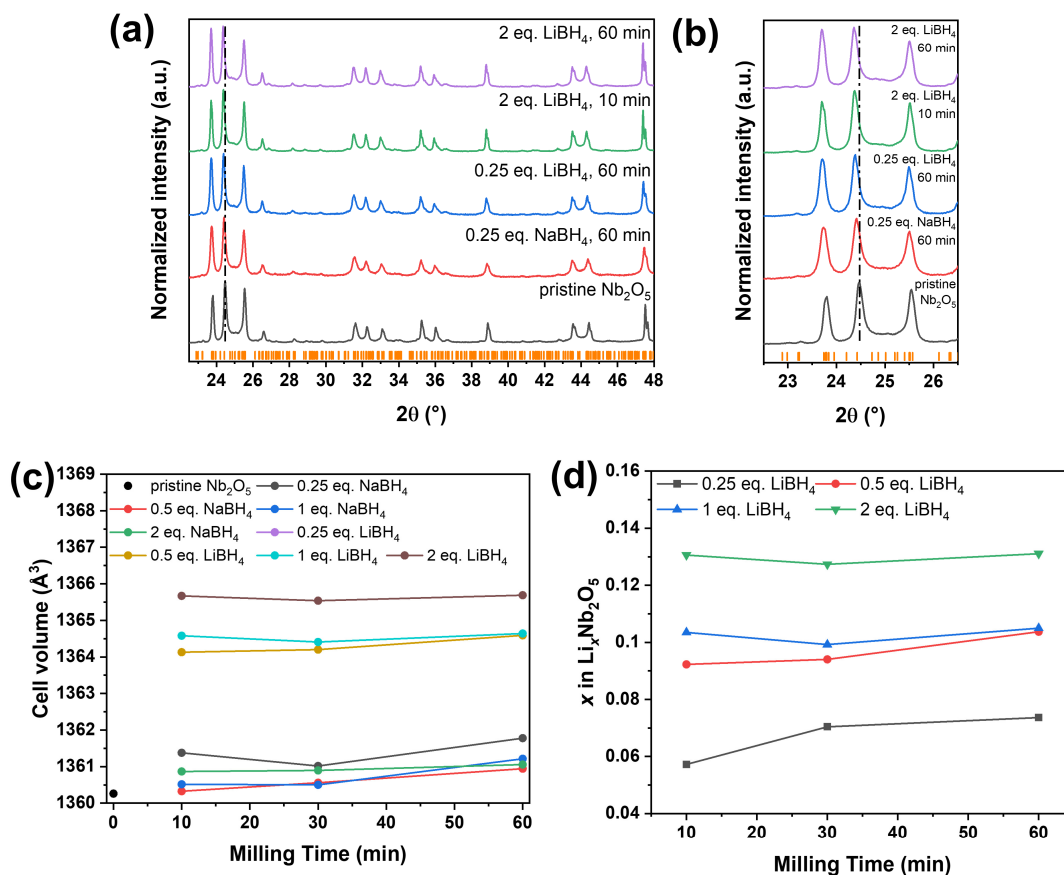


**Figure 2.** (a) PXR patterns and (b) corresponding zoom of pristine and reduced niobia. Orange ticks indicate the Bragg positions of monoclinic  $\text{Nb}_2\text{O}_5$  ( $P2_1/m$ ). The vertical line is meant for easier visualization of the shift of reflections. (c) Evolution of the cell volume of pristine  $\text{Nb}_2\text{O}_5$  compared with  $\text{LiBH}_4$ - and  $\text{NaBH}_4$ -reduced samples and (d) the estimated Li content based on Rietveld refinement assuming a sum formula of  $\text{Li}_x\text{Nb}_2\text{O}_5$  for the  $\text{LiBH}_4$ -reduced samples.

Although the microstructure parameters, crystallite size and strain, could not be refined simultaneously (Supplementary Materials, Figure S9), an overall trend could be observed in the influence of the reaction parameters on the microstructure. With increasing milling times and decreasing hydride concentrations, the niobia crystallites exhibited larger defects, which were characterized by smaller crystallite size and/or larger strain. Longer milling times tended to damage the material due to the sustained mechanical stress [39–41]. On the other hand, the decrease in damage with decreasing  $\text{NaBH}_4$  and  $\text{LiBH}_4$  suggested a mechanical buffering effect of the respective hydride, meaning that the boron hydrides could absorb some of the mechanical energy from collisions with the milling balls without decomposing. The transfer of mechanical energy was thus hindered, and less energy was available to induce the mechanochemical reduction, which also nicely explains the lighter coloration of samples prepared with high  $\text{NaBH}_4$  concentrations. In this case, the excess of hydride had the opposite effect to that of an inert grinding auxiliary such as inorganic salts, which can, for example, be added to sticky reaction mixtures to achieve a better texture and efficient mixing [42]. For comparison, milling of only  $\text{Nb}_2\text{O}_5$  for 60 min at

300 rpm did not result in significant changes in the cell volume and the microstructure (Supplementary Materials, Figure S9). It can therefore be concluded that the observed changes in the microstructure of black niobia mainly originated from the reduction process.

While clear differences in the sample coloration were observed in the NaBH<sub>4</sub>-reduced samples (the darker the samples, the higher their degree of reduction), color differences in the LiBH<sub>4</sub>-reduced samples were more subtle. This raises the question of why NaBH<sub>4</sub>-reduced samples showed larger differences in color. In fact, the higher molar mass that NaBH<sub>4</sub> necessitated nearly doubled the mass compared with that of LiBH<sub>4</sub> to achieve the same Nb<sub>2</sub>O<sub>5</sub>-to-hydride ratio; for instance, 0.8539 g of NaBH<sub>4</sub> was required for a 1:2 ratio, while only 0.4920 g of LiBH<sub>4</sub> was needed. Consequently, it is very likely that LiBH<sub>4</sub> showed the same overall behavior, but it was less obvious due to the lower mass used. Theoretically, the use of an even greater excess of LiBH<sub>4</sub> should therefore lead to a lower degree of reduction.

To test this hypothesis, Nb<sub>2</sub>O<sub>5</sub> was milled with an excess of 5 eq. LiBH<sub>4</sub> (similar weight ratio of the reactants than Nb<sub>2</sub>O<sub>5</sub>/2 eq. NaBH<sub>4</sub>) for 10 min at 300 rpm, with 200 µL of DME added to prevent cementation. The resulting light blue oxide was significantly lighter than the sample obtained with only two equivalents of LiBH<sub>4</sub> under identical milling conditions. After washing and removal of unreacted LiBH<sub>4</sub>, a cell volume of 1364.46 Å<sup>3</sup> was determined by Rietveld refinement. The lighter coloration and reduced cell volume suggested that a lower degree of reduction was achieved with the excess LiBH<sub>4</sub>. Consequently, the above hypothesis was confirmed and higher concentrations of the two alkali metal borohydrides tested led to an overall lower reduction as the excess hydride acted as a buffer material.

### 3.3. Solid-State NMR Spectroscopy

Solid-state NMR spectroscopy was applied to study the effectiveness of the washing process, which was needed to remove unreacted hydrides and other possibly formed boron-containing side-products such as alkali metal borates [43,44], which could also be envisioned, in addition to the formation of volatile boron-containing side-products. Moreover, the local environment of intercalated lithium could then be investigated.

As shown in the <sup>11</sup>B and <sup>7</sup>Li solid-state MAS NMR spectra of the pristine LiBH<sub>4</sub> starting material, an intense central  $|+1/2\rangle \leftrightarrow |-1/2\rangle$  transition was observed at  $-42.0$  and  $-0.7$  ppm, respectively, as well as a spinning sideband manifold originating from the outer satellite transitions  $|\pm 1/2\rangle \leftrightarrow |\pm 3/2\rangle$  (Figure 3a, Figure 4a), which was consistent with the literature [45,46]. With the help of the DMFit software package [33] for both spectra, the quadrupolar parameter  $C_Q$  was extracted for the cases of  $\eta_Q = 0$  and 1, which hinted at the local site asymmetry and coordination environment (Supplementary Materials, Table S1). The <sup>11</sup>B solid-state NMR spectra showed the broad signal of the probe head, which contained a B-containing stator, so the signals could only be interpreted to a limited extent.

After ball milling to reduce Nb<sub>2</sub>O<sub>5</sub> with 0.25 eq. LiBH<sub>4</sub> for 60 min, the <sup>11</sup>B spectrum mainly showed the signal of the probe head of the NMR device and no signal of pristine LiBH<sub>4</sub> was detected at  $-42.0$  ppm. In addition, one could clearly see the structured signal of small spinning sidebands centered around 0.2 ppm and a broader shoulder at around 10 ppm, indicating the presence of an unknown, possibly partially oxidized, boron species in the sample, but only in very small amounts (Figure 3b). This became clear when comparing the intensities to the spectrum of LiBH<sub>4</sub> (shown in Figure 3a) in which the signal of the probe head was almost completely suppressed. However, as shown in Figure 3c, the LiBH<sub>4</sub> starting material exhibited signals in the same region, which would match with tetrahedral BO<sub>4</sub> (around 0 ppm) and trigonal BO<sub>3</sub> (around 10 ppm) units [43,47]. Therefore, it cannot definitely be determined whether they formed during the reduction process or

were simply present in the starting material. Irrespective, their overall concentration was very low, which agreed with the low degree of reduction.

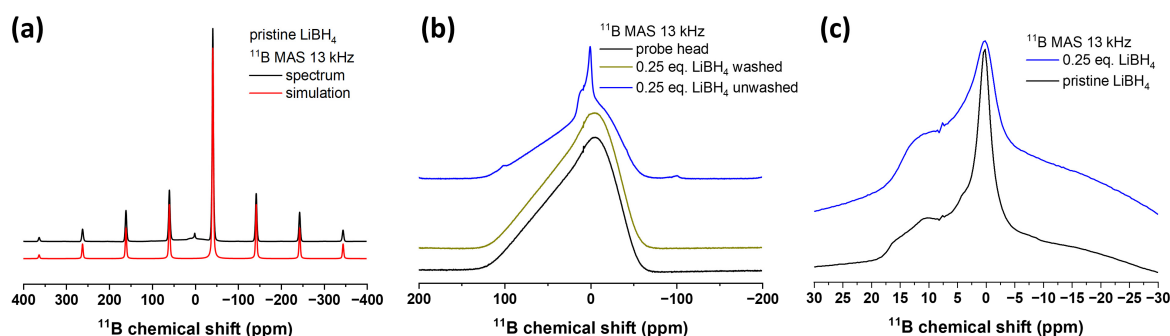


**Figure 3.** (a)  $^{11}\text{B}$  MAS NMR spectra (black) of  $\text{LiBH}_4$  and fitted with a single Gaussian–Lorentz line (red). (b) Normalized  $^{11}\text{B}$  MAS NMR of the probe head measured with an empty rotor (black) in comparison with the washed (yellow) and unwashed (blue)  $\text{Nb}_2\text{O}_5$  reduced with 0.25 eq.  $\text{LiBH}_4$  for 60 min. (c) Comparison of the magnified oxidic boron–containing side-phases present in pristine  $\text{LiBH}_4$  (black) and in  $\text{Nb}_2\text{O}_5$  reduced with 0.25 eq.  $\text{LiBH}_4$  for 60 min (blue). For better comparison, both spectra are normalized to their respective intensity value at 0.12 ppm.

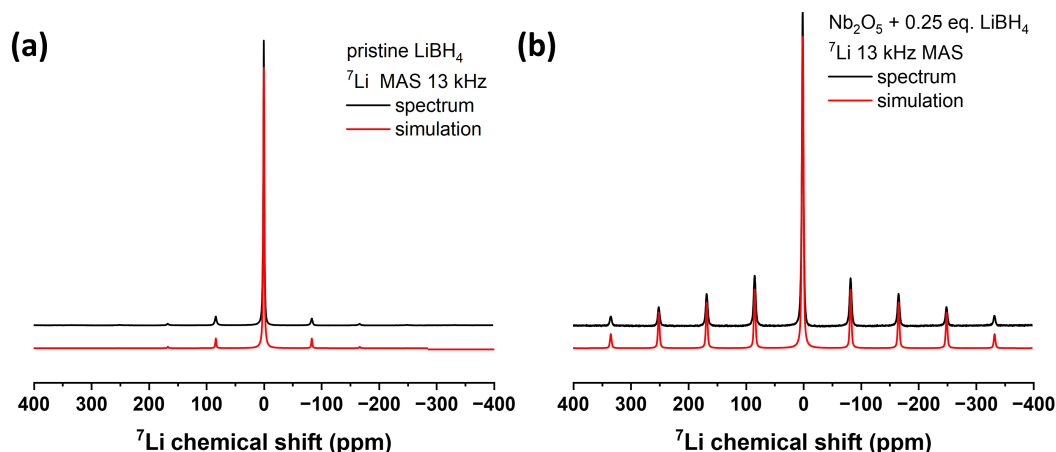


**Figure 4.** (a)  $^7\text{Li}$  MAS NMR spectra (black) of  $\text{LiBH}_4$  and fitted with a single Gaussian–Lorentz line (red). (b) Corresponding  $^7\text{Li}$  MAS NMR spectrum of the washed and reduced niobia sample (black) and fitted with a single Gaussian–Lorentz line (red).

After washing, the spinning sidebands were no longer visible, indicating that all boron species were successfully removed by washing with water (Figure 3c). Regarding the  $^7\text{Li}$  spectrum of  $\text{Nb}_2\text{O}_5$  reduced with 0.25 eq.  $\text{LiBH}_4$  for 60 min, all the features discussed above, in line with the Li incorporation into the  $\text{Nb}_2\text{O}_5$ , were visible in the spectrum (Figure 4b). The  $C_Q$  parameter obtained was different from that of  $\text{LiBH}_4$  (Supplementary Materials, Table S1), which was qualitatively already clear due to the differences in the range. The intensity profile of the spinning sideband diversity underlined the different crystallographic environment of the Li atom in  $\text{LiBH}_4$  and the reduced  $\text{Nb}_2\text{O}_5$ . Ball milling  $\text{Nb}_2\text{O}_5$  with 2 eq.  $\text{LiBH}_4$  led to almost identical  $^7\text{Li}$  spectra (Supplementary Materials, Figures S10 and S11).

The examples in Figure 4 are representative of the study. Two additional  $^7\text{Li}$  spectra are shown in the Supplementary Materials (Figures S10 and S11) and look almost identical to those presented here, indicating that the milling conditions do not appear to have a significant influence on the chemical environment of the lithium nucleus after reduction.

Regarding the  $^{11}\text{B}$  solid-state MAS NMR of pristine  $\text{NaBH}_4$ , a featureless intense central transition at  $-42$  ppm was observed (Supplementary Materials, Figure S12a), in

accordance with literature [46]. Again, an additional signal at  $\sim 3$  ppm showed the presence of unknown oxidic boron-containing species already in the starting material [44,48]. In contrast to the  $\text{LiBH}_4$  niobia-reduced sample, large amounts of unreacted  $\text{NaBH}_4$  were still detected in the  $^{11}\text{B}$  MAS spectrum after ball milling  $\text{Nb}_2\text{O}_5$  and 0.25 eq.  $\text{NaBH}_4$  for 60 min, which were successfully removed during the washing process (Supplementary Materials, Figure S12b). The presence of unreacted  $\text{NaBH}_4$  in the as-milled sample indicated a lower conversion compared to the use of  $\text{LiBH}_4$  as a reducing agent.

Overall, no significant amounts of solid boron-containing side-products were detected that could be clearly identified as side-products of the reaction. Suspending the reaction mixture in deuterated acetonitrile after milling and analyzing the solution by NMR also gave no clear evidence of the formation of higher boranes or other soluble boron-containing species. On the other hand, the degree of reduction was rather low, especially with  $\text{NaBH}_4$  as reducing agent, meaning that only small amounts of side-products were to be expected. The low degree of reduction, the observed buffering effect, and the rather complicated question of the formation of boron-containing by-products are less favorable compared with the use of alkali metal hydrides as reducing agents [28].

### 3.4. Raman and UV–Vis Absorbance Spectroscopy

Raman spectroscopy was additionally employed to study structural changes during milling. As shown in Figure 5a, all typical bands of monoclinic  $\text{H-Nb}_2\text{O}_5$  remained detectable for both  $\text{NaBH}_4$ - and  $\text{LiBH}_4$ -reduced and washed samples. These included Nb-O-Nb angle-deformations between 160 to  $300\text{ cm}^{-1}$ , transverse optic (TO) modes originating from symmetric stretching of  $\text{NbO}_6$  octahedra between 600 and  $700\text{ cm}^{-1}$ , and the longitudinal optic (LO) mode of  $\text{NbO}_6$  edge-shared octahedra at around  $990\text{ cm}^{-1}$  [42]. After mechanochemical reduction, a significant decrease in Raman activity and broadening of the observed bands (Figure 5a), as well as a red shift of the LO mode to up to  $885\text{ cm}^{-1}$  were noted. These results are in good agreement with Rietveld refinement, as reduced crystallite sizes and increased strain typically lead to broadened peaks and peak shifts [49,50]. Additionally, these changes, which are often reported in literature for such partially reduced systems, can also be induced by structural disorder and point defects such as oxygen vacancies [11,12,21]. Although it is not possible to identify the exact origin of the changes in the Raman spectra, which were most likely due to a combination of several factors, it can be concluded that the use of  $\text{LiBH}_4$  led to a stronger reduction and a greater structural disorder, as the Raman signals were broadened and shifted compared with  $\text{NaBH}_4$ -reduced samples.

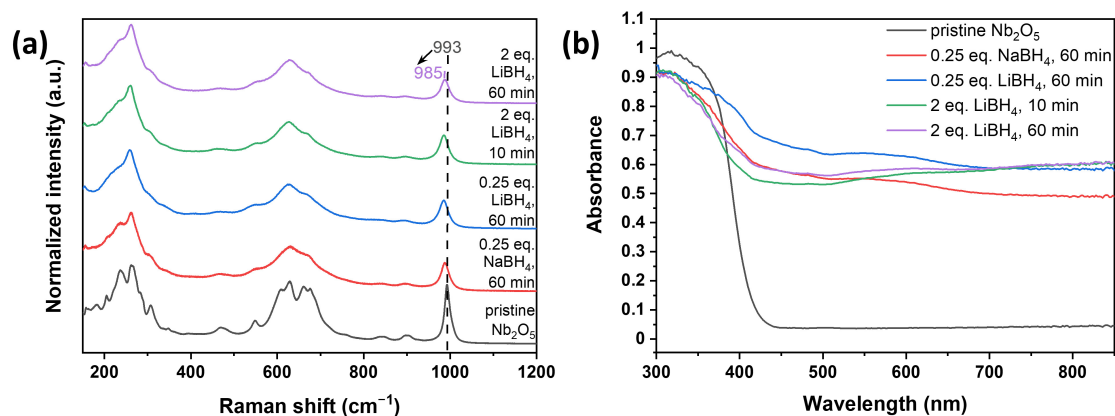


**Figure 5.** (a) Raman spectra of pristine (black)  $\text{Nb}_2\text{O}_5$  and with  $\text{NaBH}_4$ - (0.25 eq./60 min, red) and  $\text{LiBH}_4$  (0.25 eq./60 min, blue; 2 eq./10 min, green; 2 eq./60 min, purple) reduced  $\text{Nb}_2\text{O}_5$ . Corresponding DRS-UV-Vis absorbance spectra of pristine and reduced niobia are shown in (b).

Similarly, the optical properties were also affected by the mechanochemical reduction process. While the diffuse reflectance UV–Vis (DRS–UV–Vis) spectrum of pristine  $\text{Nb}_2\text{O}_5$  showed only UV absorption with negligible absorbance in the visible and near-infrared (NIR) regions, all reduced samples demonstrated significantly enhanced absorption in these regions (Figure 5b), as well as a decrease in the optical band gap of up to 0.4 eV, as determined using the Kubelka–Munk function (Supplementary Materials, Figure S13, Table S2). These optical changes can be attributed to the successful partial reduction and the introduction of defects leading to additional electronic states within the band gap, which are commonly observed for partially reduced transition metal oxides [11,12,26].

### 3.5. Photocatalytic Degradation of Methylene Blue

The enhancement of absorption properties across a broader wavelength range and the reduction of the optical band gap often enhance (photogenerated) charge carrier properties, such as improved lifetime and reduced recombination rates, leading to increased photocatalytic activity [26]. This effect has also been observed by us for LiH-reduced samples [28]. Consequently, the photocatalytic activity of the borohydride-reduced samples was evaluated through the degradation of methylene blue (MB), a common pollutant in textile wastewater [51]. The photocatalytic degradation was tested under UV irradiation (365 nm) and visible light (400–700 nm, with the strongest irradiance being at around 450 and 550 nm). Control experiments without catalysts only showed minimal MB photobleaching (Figure 6), while stirring MB with the photocatalyst in the absence of light also did not significantly reduce its concentration (Figure 6b).

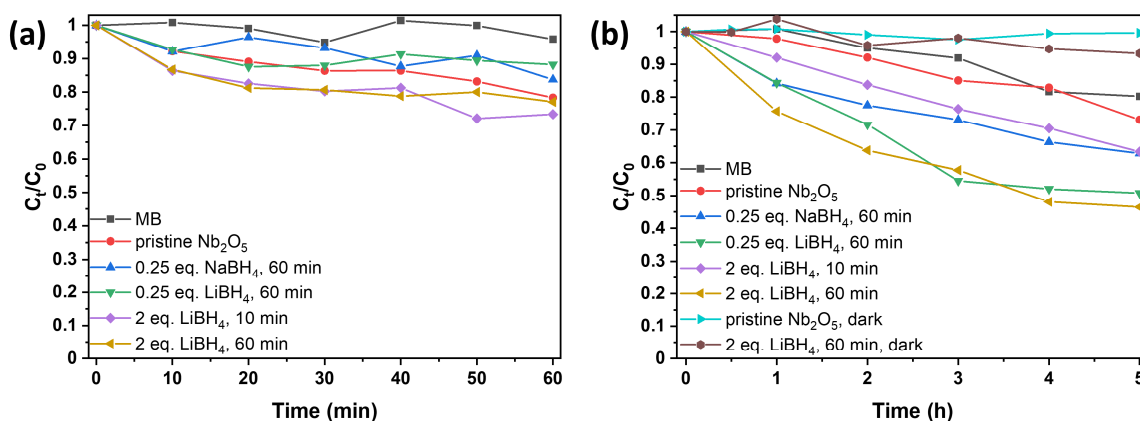


**Figure 6.** Photocatalytic degradation of methylene blue (MB) (a) under UV (365 nm) and (b) under visible light without catalyst (black), with pristine niobia (red) and with reduced niobia (blue: 0.25 eq.  $\text{NaBH}_4$ , 60 min; green: 0.25 eq.  $\text{LiBH}_4$ , 60 min; purple: 2 eq.  $\text{LiBH}_4$ , 10 min; yellow: 2 eq.  $\text{LiBH}_4$ , 60 min). In (b), MB and  $\text{Nb}_2\text{O}_5$  (turquoise), as well as  $\text{LiBH}_4$ -reduced  $\text{Nb}_2\text{O}_5$  (brown) were also stirred without illumination for comparison with stirring with illumination. Note the different time scales between (a) and (b).

Under UV light, both pristine and reduced niobia showed almost no activity as only 10 to 30% of MB was degraded after 60 min, depending on the synthesis conditions of the catalyst (Figure 6a). While the photocatalytic activity of the samples prepared with 2 eq.  $\text{LiBH}_4$  showed a slight improvement compared with the pristine material, both pristine and black niobia were less effective as UV photocatalysts compared with our previously synthesized black titania samples [28]. In contrast, all tested black niobia samples showed enhanced performance under visible light compared with the pristine material. While pristine  $\text{Nb}_2\text{O}_5$  degraded only 27% of MB in five hours, the degradation was improved to 37% when using the samples prepared with 0.25 eq.  $\text{NaBH}_4$ /60 min (blue) and 2 eq.  $\text{LiBH}_4$ /10 min (purple), as shown in Figure 6b. Further milling with 0.25 (green) and 2 eq.

(yellow)  $\text{LiBH}_4$  resulted in 49 and 53% degradation, respectively, which is comparable to our LiH-reduced material [28].

These findings indicate that the partial mechanochemical reduction using alkali metal boron hydrides effectively enhanced the photocatalytic properties of  $\text{Nb}_2\text{O}_5$ . Overall, the use of  $\text{LiBH}_4$  as the more effective reducing agent, higher initial hydride concentrations, and longer milling times favored the faster photocatalytic degradation of MB. This can be attributed to the partial reduction to  $\text{Nb}^{4+}$  and the increased presence of defects and structural disorder, resulting in an enhanced light absorption across a wide range of wavelengths, reduced optical band gap, and likely decreased recombination rate of photogenerated electron-hole pairs [26,52].

#### 4. Conclusions

In summary, the mechanochemical partial reduction of H- $\text{Nb}_2\text{O}_5$  using  $\text{LiBH}_4$  and  $\text{NaBH}_4$  as reducing agents at room temperature was systematically investigated, revealing a strong dependence on the type of the reducing agent. Due to a buffering effect regarding the transferred mechanical energy, large boron hydride concentrations did not benefit the reduction process. Structural analysis by PXRD measurements confirmed the retention of the  $\text{Nb}_2\text{O}_5$  lattice, with  $\text{Li}^+$  intercalation leading to an increase in cell volume, as also supported by  $^7\text{Li}$  NMR spectroscopy. All reduced samples demonstrated enhanced visible light absorption and a band gap reduction of up to 0.4 eV compared with pristine niobia. Raman spectroscopy revealed increasing structural disorder due to the formation of defects, particularly for the stronger-reduced  $\text{LiBH}_4$  samples. These defects contributed to significantly improved photocatalytic performance of the synthesized materials compared with pristine oxides under visible light illumination.

**Supplementary Materials:** The following supporting information can be downloaded at: <https://www.mdpi.com/article/10.3390/solids6020026/s1>, Figure S1: Photographs of  $\text{Nb}_2\text{O}_5$  reduced with different amounts of  $\text{NaBH}_4$  and  $\text{LiBH}_4$  for different milling times; Figure S2: Rietveld refinement of monoclinic H- $\text{Nb}_2\text{O}_5$  milled with 0.25 eq.  $\text{NaBH}_4$  for 10 min. Figures of merit:  $R_{wp} = 8.86$ ,  $\text{GOF} = 4.19$ ; Figure S3: Rietveld refinement of monoclinic H- $\text{Nb}_2\text{O}_5$  milled with 0.25 eq.  $\text{NaBH}_4$  for 60 min. Figures of merit:  $R_{wp} = 5.24$ ,  $\text{GOF} = 2.48$ ; Figure S4: Rietveld refinement of monoclinic H- $\text{Nb}_2\text{O}_5$  milled with 2 eq.  $\text{NaBH}_4$  for 60 min. Figures of merit:  $R_{wp} = 7.72$ ,  $\text{GOF} = 3.66$ ; Figure S5: Rietveld refinement of monoclinic H- $\text{Nb}_2\text{O}_5$  milled with 0.25 eq.  $\text{LiBH}_4$  for 60 min. Figures of merit:  $R_{wp} = 7.11$ ,  $\text{GOF} = 2.49$ ; Figure S6: Rietveld refinement of monoclinic H- $\text{Nb}_2\text{O}_5$  milled with 2 eq.  $\text{LiBH}_4$  for 10 min. Figures of merit:  $R_{wp} = 10.65$ ,  $\text{GOF} = 5.57$ ; Figure S7: Rietveld refinement of monoclinic H- $\text{Nb}_2\text{O}_5$  milled with 2 eq.  $\text{LiBH}_4$  for 60 min. Figures of merit:  $R_{wp} = 9.39$ ,  $\text{GOF} = 4.91$ ; Figure S8: Rietveld refinement of monoclinic H- $\text{Nb}_2\text{O}_5$  milled with 5 eq.  $\text{LiBH}_4$  for 10 min. Figures of merit:  $R_{wp} = 9.39$ ,  $\text{GOF} = 4.91$ ; Figure S9: Evolution of the crystallite size as a function of milling time and (a)  $\text{NaBH}_4$  and (b)  $\text{LiBH}_4$  concentration, when only the crystallite size was refined. Analogous evolution of (c), (d) crystallite size and (e), (f) strain as a function of milling time and hydride concentration, when both the crystallite size and the strain were refined. To accommodate experimental errors, the standard deviation of the strain calculated by Topas was multiplied by a factor of three; Figure S10:  $^7\text{Li}$  MAS NMR spectrum of  $\text{Nb}_2\text{O}_5 + \text{LiBH}_4$  (1:2) after 10 min with a single line shape simulation; Figure S11:  $^7\text{Li}$  MAS NMR spectrum of  $\text{Nb}_2\text{O}_5 + \text{LiBH}_4$  (1:2) after 60 min with a single line shape simulation; Table S1: Summary of the  $^7\text{Li}$  and  $^{11}\text{B}$  solid-state NMR spectroscopic observables obtained for  $\text{LiBH}_4$ - and three selected samples of  $\text{LiBH}_4$ -reduced  $\text{Nb}_2\text{O}_5$  extracted from the DMFit software with  $\delta$  being the observed resonance (in ppm) and  $C_Q$  being the quadrupolar parameter (in kHz) refined for  $\eta_Q = 0$  and 1; Figure S12: (a)  $^{11}\text{B}$  MAS NMR of pristine  $\text{NaBH}_4$ . (b)  $^{11}\text{B}$  MAS NMR of the probe head measured with an empty rotor (black) in comparison to the washed (yellow) and unwashed (blue)  $\text{Nb}_2\text{O}_5$  reduced with 0.25 eq.  $\text{NaBH}_4$  for 60 min; Figure S13: Kubelka–Munk plot of pristine  $\text{Nb}_2\text{O}_5$  (black) and with  $\text{NaBH}_4$  (0.25 eq./60 min, red) and  $\text{LiBH}_4$  (0.25 eq./60 min, blue; 2 eq./10 min, green; 2 eq./60 min,

purple) reduced Nb<sub>2</sub>O<sub>5</sub>; Table S2: Optical band gaps of pristine and reduced niobia determined using the Kubelka–Munk function. [39–41,53–55].

**Author Contributions:** Conceptualization, A.M. and G.K.; methodology, A.M. and E.C.J.G.; investigation, A.M.; resources, G.K.; writing—original draft preparation, A.M.; writing—review and editing, E.C.J.G. and G.K.; supervision, G.K.; project administration, G.K.; funding acquisition, G.K. All authors have read and agreed to the published version of the manuscript.

**Funding:** Instrumentation and technical assistance for this work were provided by the Service Center X-ray Diffraction, with financial support from Saarland University and German Science Foundation (project number INST 256/349-1).

**Data Availability Statement:** The original contributions presented in the study are included in the article/Supplementary Materials. Further inquiries can be directed to the corresponding author.

**Acknowledgments:** We thank Petra Herbeck-Engel from the INM-Leibniz Institute for New Materials, Saarbrücken, for Raman measurements, as well as Clemens Matt and Haakon Wiedemann, Physical Chemistry and Chemistry Education, Saarland University, for continuous-wave EPR measurements.

**Conflicts of Interest:** The authors declare no conflicts of interest.

## References

1. Cava, R.J.; Murphy, D.W.; Zahurak, S.M. Lithium Insertion in Wadsley-Roth Phases Based on Niobium Oxide. *J. Electrochem. Soc.* **1983**, *130*, 2345–2351. [CrossRef]
2. Soares, M.R.N.; Leite, S.; Nico, C.; Peres, M.; Fernandes, A.J.S.; Graça, M.P.F.; Matos, M.; Monteiro, R.; Monteiro, T.; Costa, F.M. Effect of processing method on physical properties of Nb<sub>2</sub>O<sub>5</sub>. *J. Eur. Ceram. Soc.* **2011**, *31*, 501–506. [CrossRef]
3. Le Viet, A.; Reddy, M.V.; Jose, R.; Chowdari, B.V.R.; Ramakrishna, S. Nanostructured Nb<sub>2</sub>O<sub>5</sub> Polymorphs by Electrospinning for Rechargeable Lithium Batteries. *J. Phys. Chem. C* **2010**, *114*, 664–671. [CrossRef]
4. Graça, M.P.F.; Meireles, A.; Nico, C.; Valente, M.A. Nb<sub>2</sub>O<sub>5</sub> nanosize powders prepared by sol-gel-Structure, morphology and dielectric properties. *J. Alloys Compd.* **2013**, *553*, 177–182. [CrossRef]
5. Chambon, L.; Maleysson, C.; Pauly, A.; Germain, J.P.; Demarne, V.; Grisel, A. Investigation, for NH<sub>3</sub> gas sensing applications, of the Nb<sub>2</sub>O<sub>5</sub> semiconducting oxide in the presence of interferent species such as oxygen and humidity. *Sens. Actuator B Chem.* **1997**, *45*, 107–114. [CrossRef]
6. Chambon, L.; Pauly, A.; Germain, J.P.; Maleysson, C.; Demarne, V.; Grisel, A. A model for the responses of Nb<sub>2</sub>O<sub>5</sub> sensors to CO and NH<sub>3</sub> gases. *Sens. Actuator B Chem.* **1997**, *43*, 60–64. [CrossRef]
7. Le Viet, A.; Jose, R.; Reddy, M.V.; Chowdari, B.V.R.; Ramakrishna, S. Nb<sub>2</sub>O<sub>5</sub> photoelectrodes for dye-sensitized solar cells: Choice of the polymorph. *J. Phys. Chem. C* **2010**, *114*, 21795–21800. [CrossRef]
8. Su, K.; Liu, H.; Gao, Z.; Fornasiero, P.; Wang, F. Nb<sub>2</sub>O<sub>5</sub>-Based Photocatalysts. *Adv. Sci.* **2021**, *8*, 2003156. [CrossRef]
9. Chen, X.; Liu, L.; Huang, F. Black titanium dioxide (TiO<sub>2</sub>) nanomaterials. *Chem. Soc. Rev.* **2015**, *44*, 1861–1885. [CrossRef]
10. Chen, X.; Liu, L.; Yu, P.Y.; Mao, S.S. Increasing Solar Absorption for Photocatalysis with Black Hydrogenated Titanium Dioxide Nanocrystals. *Science* **2011**, *331*, 746–750. [CrossRef]
11. Cui, H.; Zhu, G.; Xie, Y.; Zhao, W.; Yang, C.; Lin, T.; Gu, H.; Huang, F. Black nanostructured Nb<sub>2</sub>O<sub>5</sub> with improved solar absorption and enhanced photoelectrochemical water splitting. *J. Mater. Chem. A* **2015**, *3*, 11830–11837. [CrossRef]
12. Zhao, W.; Zhao, W.; Zhu, G.; Lin, T.; Xu, F.; Huang, F. Black Nb<sub>2</sub>O<sub>5</sub> nanorods with improved solar absorption and enhanced photocatalytic activity. *Dalton Trans.* **2016**, *45*, 3888–3894. [CrossRef] [PubMed]
13. Sinhamahapatra, A.; Jeon, J.-P.; Kang, J.; Han, B.; Yu, J.-S. Oxygen-Deficient Zirconia (ZrO<sub>2-x</sub>): A New Material for Solar Light Absorption. *Sci. Rep.* **2016**, *6*, 27218. [CrossRef] [PubMed]
14. Matsukawa, T.; Ishigaki, T. Effect of isothermal holding time on hydrogen-induced structural transitions of WO<sub>3</sub>. *Dalton Trans.* **2021**, *50*, 7590–7596. [CrossRef]
15. Badreldin, A.; Imam, M.D.; Wubulikasimu, Y.; Elsaid, K.; Abusrafa, A.E.; Balbuena, P.B.; Abdel-Wahab, A. Surface microenvironment engineering of black V<sub>2</sub>O<sub>5</sub> nanostructures for visible light photodegradation of methylene blue. *J. Alloys Compd.* **2021**, *871*, 159615. [CrossRef]
16. Kim, H.-S.; Cook, J.B.; Lin, H.; Ko, J.S.; Tolbert, S.H.; Ozolins, V.; Dunn, B. Oxygen vacancies enhance pseudocapacitive charge storage properties of MoO<sub>3-x</sub>. *Nat. Mater.* **2017**, *16*, 454–462. [CrossRef]
17. Tong, Z.; Yang, R.; Wu, S.; Shen, D.; Jiao, T.; Zhang, K.; Zhang, W.; Lee, C.-S. Surface-Engineered Black Niobium Oxide@Graphene Nanosheets for High-Performance Sodium-/Potassium-Ion Full Batteries. *Small* **2019**, *15*, 1901272. [CrossRef]

18. Lin, X.; Xia, S.; Zhang, L.; Zhang, Y.; Sun, S.; Chen, Y.; Chen, S.; Ding, B.; Yu, J.; Yan, J. Fabrication of Flexible Mesoporous Black Nb<sub>2</sub>O<sub>5</sub> Nanofiber Films for Visible-Light-Driven Photocatalytic CO<sub>2</sub> Reduction into CH<sub>4</sub>. *Adv. Mater.* **2022**, *34*, 2200756. [[CrossRef](#)]
19. Yang, P.; Fan, Y.; Hu, K.; Jiang, L.; Tan, L.; Wang, Z.; Li, A.; Yang, S.; Hu, Y.; Gu, H. Fast, Sensitive, and Highly Selective Room-Temperature Hydrogen Sensing of Defect-Rich Orthorhombic Nb<sub>2</sub>O<sub>5-x</sub> Nanobelts with an Abnormal p-Type Sensor Response. *ACS Appl. Mater. Interfaces* **2022**, *14*, 25937–25948. [[CrossRef](#)]
20. Cheng, S.; Wang, J.; Duan, S.; Zhang, J.; Wang, Q.; Zhang, Y.; Li, L.; Liu, H.; Xiao, Q.; Lin, H. Anionic oxygen vacancies in Nb<sub>2</sub>O<sub>5-x</sub>/carbon hybrid host endow rapid catalytic behaviors for high-performance high areal loading lithium sulfur pouch cell. *Chem. Eng. J.* **2021**, *417*, 128172. [[CrossRef](#)]
21. Li, S.; Cui, Y.; Kang, R.; Zou, B.; Ng, D.H.L.; El-Khodary, S.A.; Liu, X.; Qiu, J.; Lian, J.; Li, H. Oxygen vacancies boosted the electrochemical kinetics of Nb<sub>2</sub>O<sub>5-x</sub> for superior lithium storage. *Chem. Commun.* **2021**, *57*, 8182–8185. [[CrossRef](#)] [[PubMed](#)]
22. Luo, D.; Zhang, Z.; Li, G.; Cheng, S.; Li, S.; Li, J.; Gao, R.; Li, M.; Sy, S.; Deng, Y.-P.; et al. Revealing the Rapid Electrocatalytic Behavior of Ultrafine Amorphous Defective Nb<sub>2</sub>O<sub>5-x</sub> Nanocluster toward Superior Li-S Performance. *ACS Nano* **2020**, *14*, 4849–4860. [[CrossRef](#)]
23. de Araújo, M.A.; Gromboni, M.F.; Marken, F.; Parker, S.C.; Peter, L.M.; Turner, J.; Aspinall, H.C.; Black, K.; Mascaro, L.H. Contrasting transient photocurrent characteristics for thin films of vacuum-doped “grey” TiO<sub>2</sub> and “grey” Nb<sub>2</sub>O<sub>5</sub>. *Appl. Catal. B* **2018**, *237*, 339–352. [[CrossRef](#)]
24. Tan, D.; García, F. Main group mechanochemistry: From curiosity to established protocols. *Chem. Soc. Rev.* **2019**, *48*, 2274–2292. [[CrossRef](#)]
25. Zhang, M.; Pei, Q.; Chen, W.; Liu, L.; He, T.; Chen, P. Room temperature synthesis of reduced TiO<sub>2</sub> and its application as a support for catalytic hydrogenation. *RSC Adv.* **2017**, *7*, 4306–4311. [[CrossRef](#)]
26. Ou, G.; Xu, Y.; Wen, B.; Lin, R.; Ge, B.; Tang, Y.; Liang, Y.; Yang, C.; Huang, K.; Zu, D.; et al. Tuning defects in oxides at room temperature by lithium reduction. *Nat. Commun.* **2018**, *9*, 1302. [[CrossRef](#)]
27. Zhou, X.; Liu, N.; Schmidt, J.; Kahnt, A.; Osvet, A.; Romeis, S.; Zolnhofer, E.M.; Marthala, V.R.R.; Guldi, D.M.; Peukert, W.; et al. Noble-Metal-Free Photocatalytic Hydrogen Evolution Activity: The Impact of Ball Milling Anatase Nanopowders with TiH<sub>2</sub>. *Adv. Mater.* **2017**, *29*, 1604747. [[CrossRef](#)]
28. Michaely, A.; Janka, O.; Gießelmann, E.C.J.; Haberkorn, R.; Wiedemann, H.T.A.; Kay, C.W.M.; Kickelbick, G. Black Titania and Niobia within Ten Minutes—Mechanochemical Reduction of Metal Oxides with Alkali Metal Hydrides. *Chem. Eur. J.* **2023**, *29*, e202300223. [[CrossRef](#)] [[PubMed](#)]
29. Bruker AXS Inc. *Tpoas*, Version 5; Bruker AXS Inc.: Karlsruhe, Germany, 2014.
30. Cheary, R.W.; Coelho, A.A.; Cline, J.P. Fundamental Parameters Line Profile Fitting in Laboratory Diffractometers. *J. Res. Natl. Inst. Stand. Technol.* **2004**, *109*, 1–25. [[CrossRef](#)]
31. Villars, P.; Cenzual, K. *Pearson’s Crystal Data: Crystal Structure Database for Inorganic Compounds. Release 2022/23*; ASM International®: Materials Park, OH, USA, 2023.
32. Bruker Corp. *Topasin*; Bruker Corp.: Karlsruhe, Germany, 2008.
33. Massiot, D.; Fayon, F.; Capron, M.; King, I.; Le Calvé, S.; Alonso, B.; Durand, J.-O.; Bujoli, B.; Gan, Z.; Hoatson, G. Modelling one- and two-dimensional solid-state NMR spectra. *Magn. Reson. Chem.* **2002**, *40*, 70–76. [[CrossRef](#)]
34. Schäfer, H.; Gruehn, R.; Schulte, F. The Modifications of Niobium Pentoxide. *Angew. Chem. Int. Ed.* **1966**, *5*, 40–52. [[CrossRef](#)]
35. Sarkar, A.; Khan, G.G. The formation and detection techniques of oxygen vacancies in titanium oxide-based nanostructures. *Nanoscale* **2019**, *11*, 3414–3444. [[CrossRef](#)]
36. Santara, B.; Giri, P.K.; Imakita, K.; Fujii, M. Evidence of oxygen vacancy induced room temperature ferromagnetism in solvothermally synthesized undoped TiO<sub>2</sub> nanoribbons. *Nanoscale* **2013**, *5*, 5476–5488. [[CrossRef](#)] [[PubMed](#)]
37. Wang, J.; Li, G.; Luo, D.; Zhang, Y.; Zhao, Y.; Zhou, G.; Shui, L.; Wang, X.; Chen, Z. Engineering the Conductive Network of Metal Oxide-Based Sulfur Cathode toward Efficient and Longevous Lithium–Sulfur Batteries. *Adv. Energy Mater.* **2020**, *10*, 2002076. [[CrossRef](#)]
38. Shannon, R.D. Revised effective ionic radii and systematic studies of interatomic distances in halides and chalcogenides. *Acta Crystallogr. A* **1976**, *32*, 751–767. [[CrossRef](#)]
39. Vaishnavi Krupa, B.R.; Dasgupta, A.; Ghosh, C.; Sinha, S.K. Analysis of structural transformation in nanocrystalline Y<sub>2</sub>O<sub>3</sub> during high energy ball milling. *J. Alloys Compd.* **2022**, *900*, 163550. [[CrossRef](#)]
40. Pradhan, S.K.; Shee, S.K.; Chanda, A.; Bose, P.; De, M. X-ray studies on the kinetics of microstructural evolution of Ni<sub>3</sub>Al synthesized by ball milling elemental powders. *Mater. Chem. Phys.* **2001**, *68*, 166–174. [[CrossRef](#)]
41. Hadeif, F.; Ans, M. X-ray analysis and Rietveld refinement of ball milled Fe<sub>50</sub>Al<sub>35</sub>Ni<sub>15</sub> powder. *Surf. Interfaces* **2021**, *26*, 101303. [[CrossRef](#)]
42. Howard, J.L.; Cao, Q.; Browne, D.L. Mechanochemistry as an emerging tool for molecular synthesis: What can it offer? *Chem. Sci.* **2018**, *9*, 3080–3094. [[CrossRef](#)]

43. Kuhn, A.; Tobschall, E.; Heitjans, P. Li Ion Diffusion in Nanocrystalline and Nanoglassy  $\text{LiAlSi}_2\text{O}_6$  and  $\text{LiBO}_2$ —Structure-Dynamics Relations in Two Glass Forming Compounds. *Z. Phys. Chem.* **2009**, *223*, 1359–1377. [[CrossRef](#)]
44. Lang, C.; Jia, Y.; Liu, J.; Wang, H.; Ouyang, L.; Zhu, M.; Yao, X.  $\text{NaBH}_4$  regeneration from  $\text{NaBO}_2$  by high-energy ball milling and its plausible mechanism. *Int. J. Hydrogen Energy* **2017**, *42*, 13127–13135. [[CrossRef](#)]
45. Arnbjerg, L.M.; Ravnsbæk, D.B.; Filinchuk, Y.; Vang, R.T.; Cerenius, Y.; Besenbacher, F.; Jørgensen, J.-E.; Jakobsen, H.J.; Jensen, T.R. Structure and Dynamics for  $\text{LiBH}_4$ – $\text{LiCl}$  Solid Solutions. *Chem. Mater.* **2009**, *21*, 5772–5782. [[CrossRef](#)]
46. Łodziana, Z.; Błoński, P.; Yan, Y.; Rentsch, D.; Remhof, A. NMR Chemical Shifts of  $^{11}\text{B}$  in Metal Borohydrides from First-Principle Calculations. *J. Phys. Chem. C* **2014**, *118*, 6594–6603. [[CrossRef](#)]
47. Kroeker, S.; Stebbins, J.F. Three-coordinated Boron-11 chemical shifts in borates. *Inorg. Chem.* **2001**, *40*, 6239–6246. [[CrossRef](#)]
48. Weiss, J.W.E.; Bryce, D.L. A solid-state  $^{11}\text{B}$  NMR and computational study of boron electric field gradient and chemical shift tensors in boronic acids and boronic esters. *J. Phys. Chem. A* **2010**, *114*, 5119–5131. [[CrossRef](#)] [[PubMed](#)]
49. Deluca, M.; Hu, H.; Popov, M.N.; Spitaler, J.; Dieing, T. Advantages and developments of Raman spectroscopy for electroceramics. *Commun. Mater.* **2023**, *4*, 78. [[CrossRef](#)]
50. Zuo, J.; Xu, C.; Liu, Y.; Qian, Y. Crystallite size effects on the Raman spectra of  $\text{Mn}_3\text{O}_4$ . *Nanostruct. Mater.* **1998**, *10*, 1331–1335. [[CrossRef](#)]
51. Oladoye, P.O.; Ajiboye, T.O.; Omotola, E.O.; Oyewola, O.J. Methylene blue dye: Toxicity and potential elimination technology from wastewater. *Results Eng.* **2022**, *16*, 100678. [[CrossRef](#)]
52. Sinhamahapatra, A.; Jeon, J.-P.; Yu, J.-S. A new approach to prepare highly active and stable black titania for visible light-assisted hydrogen production. *Energy Environ. Sci.* **2015**, *8*, 3539–3544. [[CrossRef](#)]
53. Balogh, L.; Ribárik, G.; Ungár, T. Stacking faults and twin boundaries in fcc crystals determined by x-ray diffraction profile analysis. *J. Appl. Phys.* **2006**, *100*, 023512. [[CrossRef](#)]
54. Budak, Ö.; Geißler, M.; Becker, D.; Kruth, A.; Quade, A.; Haberkorn, R.; Kickelbick, G.; Etzold, B.J.M.; Presser, V. Carbide-Derived Niobium Pentoxide with Enhanced Charge Storage Capacity for Use as a Lithium-Ion Battery Electrode. *ACS Appl. Energy Mater.* **2020**, *3*, 4275–4285. [[CrossRef](#)]
55. Catti, M.; Ghaani, M.R. On the lithiation reaction of niobium oxide: Structural and electronic properties of  $\text{Li}_{1.714}\text{Nb}_2\text{O}_5$ . *Phys. Chem. Chem. Phys.* **2014**, *16*, 1385–1392. [[CrossRef](#)] [[PubMed](#)]

**Disclaimer/Publisher’s Note:** The statements, opinions and data contained in all publications are solely those of the individual author(s) and contributor(s) and not of MDPI and/or the editor(s). MDPI and/or the editor(s) disclaim responsibility for any injury to people or property resulting from any ideas, methods, instructions or products referred to in the content.